J. Fluid Mech. (1999), *vol.* 396, *pp.* 183–201. Printed in the United Kingdom

Numerical study of internal wave reflection from sloping boundaries

By A. JAVAM[1], J. IMBERGER[2] AND S. W. ARMFIELD[1]

[1] Department of Mechanical Engineering, University of Sydney, Sydney, NSW 2006, Australia

[2] Department of Environmental Engineering, Centre for Water Research, University of Western Australia, Nedlands, WA 6907, Australia

(Received 19 June 1996 and in revised form 6 May 1999)

The breaking of internal waves propagating in a stratified fluid of constant buoyancy frequency on a sloping boundary was investigated numerically. It was found that at the boundary, nonlinear non-resonant interactions between the incident and reflected waves produced higher-mode waves. These modes had frequencies greater than the local buoyancy frequency and so could not radiate from the interaction region. The energy level of trapped waves increased with time and subsequently led to overturning of the density field. At the critical frequency, when the reflected wave propagated in a direction parallel to the slope, wave overturning occurred near the wall, but the point of overturning moved off the bottom as the propagation angle changed away from that of the bottom slope as the waves became increasingly supercritical. The internal wave reflection coefficient generally increased as the effects of nonlinearity and viscosity decreased, but depended strongly on the forcing frequency and the angle of the sloping boundary.

1. Introduction

Internal wave reflection from a sloping boundary has been well documented (e.g. Phillips 1977) and its importance as a source of energy for turbulence in the benthic boundary layer in lakes, oceans and estuaries has also been pointed out in connection with field observations (Armi 1978; Gregg & Sanford 1980; Eriksen 1982, 1985, 1995; Thorpe 1987; Imberger 1989; Ledwell & Watson 1991), laboratory experiments (Phillips, Shyu & Salmun 1986; Ivey 1987; Ivey & Nokes 1989; Salmun, Killworth & Blundell 1991; Taylor 1993; Ivey, De Silva & Imberger 1995; De Silva, Imberger & Ivey 1997) and from analytical and numerical studies (Eriksen 1982, 1985; Garrett 1990; Slinn & Riley 1996).

In linear and inviscid theory (Phillips 1977; Imberger 1994), the following solutions for the velocity components can be found for a two-dimensional internal wave train propagating downwards in a linearly stratified fluid in which the buoyancy frequency N is constant:

$$v = q\sin(\alpha)\cos(kx + my - \omega t) = q\sin(\alpha)\cos(\phi), \tag{1.1}$$

$$u = -q\cos(\alpha)\cos(kx + my - \omega t) = -q\cos(\alpha)\cos(\phi), \tag{1.2}$$

$$p = -\rho_o q c_p \cot(\alpha)\cos(kx + my - \omega t) = -\rho_o q c_p \cot(\alpha)\cos(\phi), \tag{1.3}$$

where u and v are the horizontal and vertical velocities in the x- and y-directions, p is the pressure, q is the maximum particle speed along the ray, α is the angle of the

rays to the horizontal, k and m are the horizontal and vertical wavenumbers, ω is the wave frequency, c_p is the phase speed,

$$c_p = \frac{\omega}{\sqrt{k^2 + m^2}}, \tag{1.4}$$

and α is the angle of the ray to the horizontal given by the dispersion relationship

$$\sin\,\alpha = \frac{\omega}{N} = \frac{k}{\sqrt{k^2 + m^2}}. \tag{1.5}$$

This wave energy will be reflected at a sloping wall (figure 1) and the combined velocity field of the incident (subscript i) and the reflected (subscript r) waves may be written as

$$v = q_i \sin(\alpha)\cos(\phi_i) - q_r \sin(\alpha)\cos(\phi_r), \tag{1.6}$$

$$u = -q_i \cos(\alpha)\cos(\phi_i) - q_r \cos(\alpha)\cos(\phi_r). \tag{1.7}$$

The boundary condition at the sloping wall requires the normal velocity to vanish so that

$$v\cos\,\beta - u\sin\,\beta = q_i \cos(\phi_i)\sin(\alpha+\beta) - q_r \cos(\phi_r)\sin(\alpha-\beta) = 0, \tag{1.8}$$

where β is the angle of the wall to the horizontal. We wish to obtain a standing wave in the normal direction, therefore

$$q_i \sin(\alpha+\beta) = q_r \sin(\alpha-\beta). \tag{1.9}$$

Equation (1.8) becomes

$$\cos\,\phi_i - \cos\,\phi_r = 0, \tag{1.10}$$

which yields

$$\Delta\phi = \phi_r - \phi_i = 0, \tag{1.11}$$

indicating that there is no phase shift introduced on reflection. This is in contrast to observations of reflection at a caustic, where the waves experience a phase shift of $\pi/2$ (Javam, Imberger & Armfield 1999*a*).

The energy transported by the incident wave through a horizontal surface in one wavelength, averaged over one period T, is obtained from

$$E_i = \int_0^{2\pi/k_i}\int_0^T p_i v_i \,\mathrm{d}\eta. \tag{1.12}$$

Using (1.1) and (1.3) leads to

$$E_i = \frac{\pi}{k_i}\rho_o q_i^2 c_{pi}\cos\,\beta, \tag{1.13}$$

where c_{pi} is the phase velocity of the incident wave. Therefore, substituting from (1.9) yields a value for the reflection coefficient:

$$C_r = \frac{E_r}{E_i} = 1. \tag{1.14}$$

Hence, in linear theory energy is conserved during the reflection process. Now consider the energy density E_{dr} of the reflected wave

$$E_{dr} = \tfrac{1}{2}\rho_o q_r^2 = \tfrac{1}{2}\rho_o q_i^2 \frac{|\boldsymbol{k}_r|}{|\boldsymbol{k}_i|}, \tag{1.15}$$

so that

$$\frac{E_{dr}}{E_{di}} = \frac{\sin(\alpha+\beta)}{\sin(\alpha-\beta)}, \tag{1.16}$$

which clearly shows that as α approaches β, the energy density of the reflected wave increases. Thus, a small-amplitude incident wave may give rise to a large-amplitude reflected wave leading to nonlinear behaviour and ultimately wave overturning, an increased rate of strain and energy dissipation near the reflection site; when the reflected rays are parallel to the sloping boundary ($\alpha = \beta$), the amplification approaches infinity.

Ivey *et al.* (1995) reported laboratory experiments in continuously stratified fluids to study internal wave breaking on a 20° bottom slope over the frequency range of $0.5 < \omega/\omega_c < 2.5$ where ω_c is the critical frequency. Using observations and (1.13), they obtained the following expressions for the average dissipation over one wave cycle within the benthic boundary layer region:

$$\bar{\epsilon} = (1 - C_r)\left(\frac{3q^2}{4\pi N}\right)\sin 4\beta \cos\beta, \tag{1.17}$$

where the reflection coefficient $C_r = 1$ for perfect reflection.

De Silva *et al.* (1997) conducted an experimental study using a parameter range covering subcritical (backward reflection when the wave frequency $\omega < N\sin\beta$), critical (when the wave frequency $\omega = N\sin\beta$) and supercritical (forward reflection when the wave frequency $\omega > N\sin\beta$) frequencies in order to characterize the turbulence generated by an internal wave breaking on a sloping bed. They used a small width of the incident wave ray compared to the bed length and their observation showed that, near the critical condition, the instabilities were first initiated close to the bed. As the incident waves became progressively either subcritical or supercritical, the initiation of the instabilities occurred away from the slope. De Silva *et al.* (1997) also observed a horizontal viscous–buoyancy intrusion propagating out from the region of impingement of the internal waves on the bottom along the constant isopycnal surface.

The aim of this paper is to explore the nature of the nonlinear processes induced by internal wave breaking on a sloping boundary, to determine the reflection coefficient, to examine the distribution of the wave energy near the reflection region and finally to estimate typical dissipation values via (1.17). We focus our attention on the initiation of breakdown, where our two-dimensional model appears to successfully reveal the nature of the instability.

2. Governing equations and numerical model

The conservation of momentum, mass and volume, under the Boussinesq approximation, can be expressed in non-dimensional form as follows (see Javam, Imberger & Armfield 1999*b*):

$$\frac{\partial u}{\partial t} + Ke\left[u\frac{\partial u}{\partial x} + v\frac{\partial u}{\partial y}\right] = -\frac{\partial p}{\partial x} + Re^{-1}\nabla^2 u, \tag{2.1}$$

$$\frac{\partial v}{\partial t} + Ke\left[u\frac{\partial v}{\partial x} + v\frac{\partial v}{\partial y}\right] = -\frac{\partial p}{\partial y} - \rho + Re^{-1}\nabla^2 v + \sin(t)f(x,y), \tag{2.2}$$

$$\frac{\partial \rho}{\partial t} + Ke\left[u\frac{\partial \rho}{\partial x} + v\frac{\partial \rho}{\partial y}\right] = Ri\, v + Re^{-1}Pr^{-1}\nabla^2\rho, \tag{2.3}$$

$$\frac{\partial u}{\partial x} + \frac{\partial v}{\partial y} = 0, \tag{2.4}$$

where

$$\left.\begin{aligned} Ri &= \frac{(-g/\rho_o)(\mathrm{d}\hat{\rho}/\mathrm{d}y)}{\omega^2} = \left[\frac{N}{\omega}\right]^2, \quad Ke = Fk_x\omega^2, \\ Pr &= \frac{\nu}{\kappa}, \quad Re = \frac{\omega}{k_x^2\nu}, \quad \nabla^2 = \frac{\partial^2}{\partial x^2} + \frac{\partial^2}{\partial y^2}, \end{aligned}\right\} \tag{2.5}$$

and where $N = \left((g/\rho_o)|\mathrm{d}\hat{\rho}/\mathrm{d}y|\right)^{1/2}$ is the buoyancy frequency, u and v are the fluctuating velocity components in the directions x and y respectively, t is the time, ρ, $\hat{\rho}$ and ρ_o are the fluctuating, background and reference densities respectively, ν is the coefficient of kinematic viscosity, κ is the coefficient of thermal diffusivity, $f(x, y)\sin t$ is the momentum source used to generate internal wave beams, ω is the frequency of the momentum source, $f(x, y)$ is the dimensionless localization function, F is the amplitude of the momentum source, and k_x is the horizontal wavenumber of the standing wave-like momentum source.

The localization function $f(x, y)$ is given by

$$f(x,y) = \begin{cases} \cos(x - x_l)\exp(-300|y - y_l|^3)/4 & \text{if } |x - x_l| \leqslant \pi \\ \{\cos(x - x_l)\exp(-300|y - y_l|^3)\}/8 & \text{if } \pi < |x - x_l| \leqslant 3\pi/2 \\ 0 & \text{otherwise,} \end{cases} \tag{2.6}$$

in which x_l and y_l are the horizontal and vertical non-dimensional locations of the momentum source respectively.

To solve the equations numerically, it is advantageous to rotate the coordinate system so that the x'-axis is directed along the sloping boundary and y' is normal to x'. The following equations are for a coordinate system rotated through angle β; the primes have been dropped from the equations for convenience:

$$\frac{\partial u}{\partial t} + Ke\left[u\frac{\partial u}{\partial x} + v\frac{\partial u}{\partial y}\right] = -\frac{\partial p}{\partial x} - \rho\sin\beta + Re^{-1}\nabla^2 u + \sin(t)f(x,y)\sin\beta, \tag{2.7}$$

$$\frac{\partial v}{\partial t} + Ke\left[u\frac{\partial v}{\partial x} + v\frac{\partial v}{\partial y}\right] = -\frac{\partial p}{\partial y} - \rho\cos\beta + Re^{-1}\nabla^2 v + \sin(t)f(x,y)\cos\beta, \tag{2.8}$$

$$\frac{\partial \rho}{\partial t} + Ke\left[u\frac{\partial \rho}{\partial x} + v\frac{\partial \rho}{\partial y}\right] = Ri(u\sin\beta + v\cos\beta) + Re^{-1}Pr^{-1}\nabla^2\rho, \tag{2.9}$$

$$\frac{\partial u}{\partial x} + \frac{\partial v}{\partial y} = 0. \tag{2.10}$$

The function $f(x, y)$ in new coordinate system becomes

$$f(x,y) = \begin{cases} \cos(2\pi x_f)\exp(-300|y_f|^3)/4 & \text{if } |x - x_l| \leqslant \pi \\ \{\cos(2\pi x_f)\exp(-300|y_f|^3)\}/8 & \text{if } \pi < |x - x_l| \leqslant 3\pi/2 \\ 0 & \text{otherwise,} \end{cases} \tag{2.11}$$

where $x_f = (x - x_l)\cos\beta - (y - y_l)\sin\beta$, $y_f = (x - x_l)\sin\beta + (y - y_l)\cos\beta$.

The equations of motion (2.7)–(2.9) were solved using a SIMPLE scheme (Patankar 1980) on a non-staggered grid with a third-order QUICK discretization for the advective terms and second-order Crank–Nicolson time integration (Armfield 1991, 1994). An open boundary based on the Sommerfeld radiation condition was developed allowing waves to propagate through the boundaries with minor influence on the interior solution. A no-slip boundary condition was used for the sloping boundary. For a

α	30, 40, 45, 50
β	5, 10, 15, 20, 25, 30, 35, 40, 45, 50, 55, 60, 65, 70, 80
Re	10^5, 5×10^4, 2.5×10^4, 2×10^4, 1.8×10^4, 10^4, 5×10^3
Ke	0.0001, 0.0015, 0.02, 0.3, 0.35, 0.5, 0.7
Ri	1.7, 2.0, 2.42, 4.0
Pr	7

TABLE 1. Parameters used in the numerical simulations.

detailed description of the mathematical and numerical method and open boundary conditions, see Javam *et al.* (1999*b*).

The simulation domain of non-dimensional size $22\pi \times 20\pi$ consisted of uniform cells in the x-direction with non-dimensional size of $\Delta x = 0.1\pi$ and variable cells in the y-direction arranged to have higher resolution in the region of high shear. The mesh size at the wall was $\Delta y = 0.01\pi$ and was stretched at the rate of 3% per cell until reaching $\Delta y = 0.1\pi$, after which the stretching was eliminated. The parameters used in the simulations are listed in table 1.

A momentum source having a width of 1.5 non-dimensional wavelengths was placed in the computational domain at $0.35L_x$ in the horizontal direction and was varied between $0.35L_y$ and $0.5L_y$ to keep the ray away from the corners. L_x and L_y are the length and width of the computational domain, respectively.

3. Results

Figures 1(*a*) and 1(*b*) illustrate the basic geometry, the computational domain and the boundary conditions used in the problem. Internal wave rays were generated using a localized standing wavelike momentum source with frequency ω. The angle of propagation of the rays depended upon the momentum source frequency ω, and the background density stratification according to the dispersion relation $\omega = N \sin \alpha$. In this section we present results from numerical experiments for supercritical, subcritical and critical cases.

3.1. *Wave–boundary interaction*

3.1.1. *Reflection process through a total cycle*

The waveforms of the internal wave before and after the reflection as shown in figure 1(*b*) are plotted in figures 2 and 3; the horizontal and vertical axes are in terms of the non-dimensional length and velocity scale, respectively. In these plots the x-direction is perpendicular to the centreline of the lower right cross-arm before reflection, and again after the reflection. Thus, it is directed downwards before reflection and upwards after reflection. It follows that the phase velocity vector is pointing in the direction of increasing x. Figure 2 shows the reflection process through a wave cycle. Reflected and incident waves are in phase and have the same frequency, while the amplitude and wavenumber of the wave are amplified upon the reflection.

To examine the effect of viscosity and nonlinearity on the reflection process, simulations were performed using different Reynolds (Re) and Keulegan (Ke) numbers. The non-dimensional parameters were chosen as follows: $Pr = 7$, $Ri = 2$, $Re = 10 \times 10^4$, 5×10^4, 2×10^4, 1×10^4 and 0.5×10^4, and $Fr = 0.0001$, 0.02, and 0.3. Results indicated

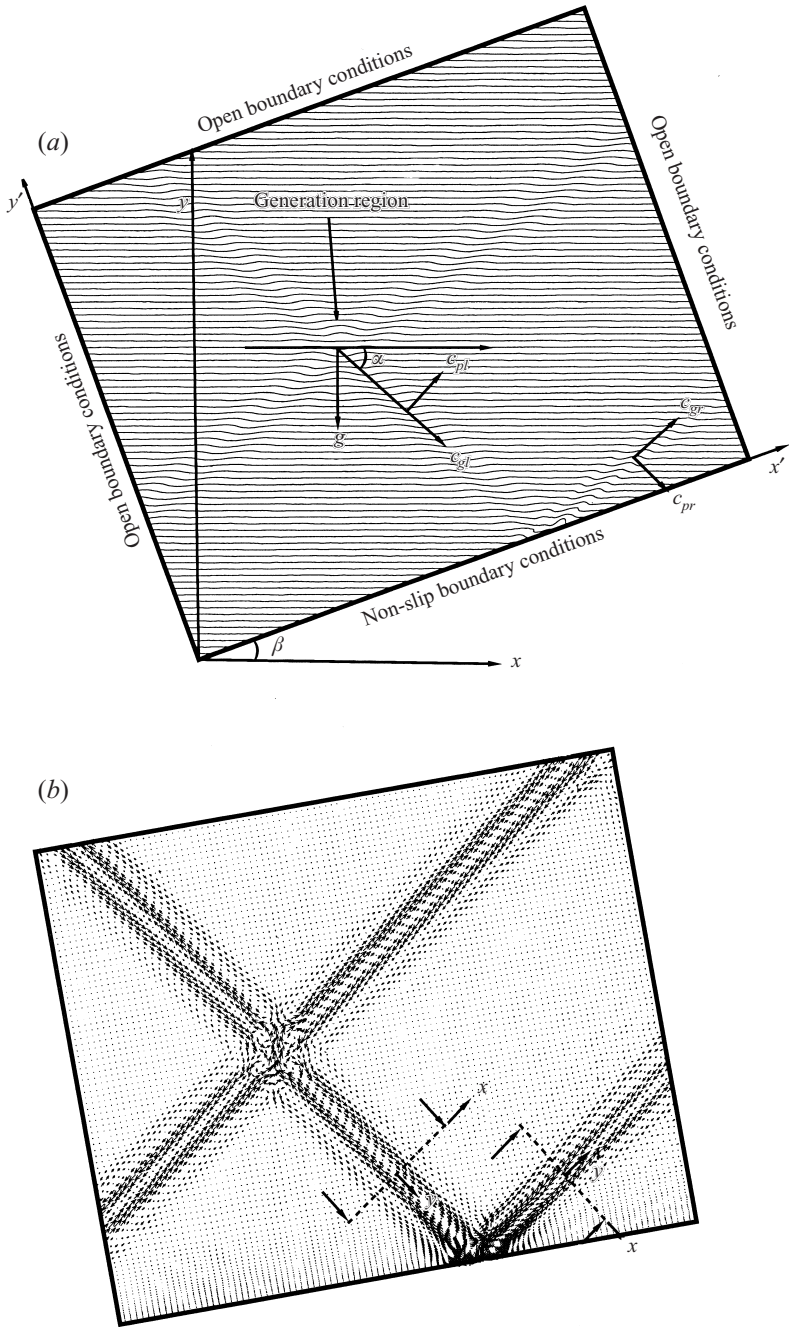

FIGURE 1. (*a*) Density contours and the geometry of internal wave reflection from the sloping boundary; $\alpha = 40$, $\beta = 20$, $Ri = 2.42$, $Ke = 0.5$, $Pr = 7$, $Re = 25\,000$. Note the change in wavenumber and wave-amplitude magnitudes on reflection. (*b*) Velocity vector plot; $\alpha = 45$, $\beta = 10$, $Ri = 2$, $Ke = 0.0001$, $Pr = 7$, $Re = 100\,000$. The cross-sections of incident and reflected waves are taken along the lines shown in this figure.

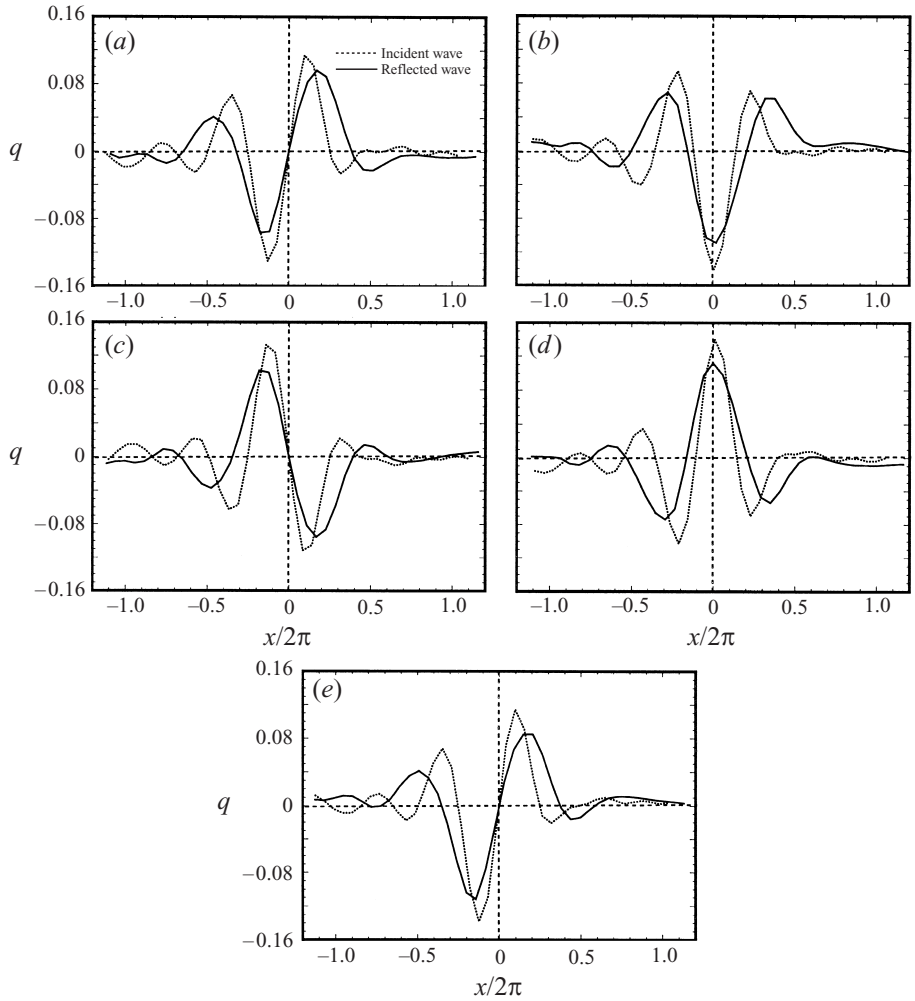

FIGURE 2. The waveforms of the internal wave before and after the reflection; $\alpha = 45$, $\beta = 10$, $Ri = 2$, $Pr = 7$. The frequency of the ray is preserved upon the reflection. In these plots the y-direction is along the group velocity and the phase velocity is pointing in the direction of increasing x. (*a*) $T = 17.0$, (*b*) $T = 17.25$, (*c*) $T = 17.5$, (*d*) $T = 17.75$, (*e*) $T = 18.0$.

that the reflected and incident waves remain in phase throughout the parameter range (figure 3); these results are in agreement with linear theory (equation (1.11)). The reflection mechanism at sloping boundaries is thus similar to reflection at a turning point, but differs from that found in caustic reflection where a phase shift of $\pi/2$ occurs (Javam *et al.* 1999*a*)

3.1.2. *Nonlinearity and viscosity effects on the reflection coefficient*

A reflection coefficient C_r defined as

$$C_r = \frac{\int^{\text{Raywidth}} p_r q_r \, \mathrm{d}\eta}{\int^{\text{Raywidth}} p_i q_i \, \mathrm{d}\eta} \tag{3.1}$$

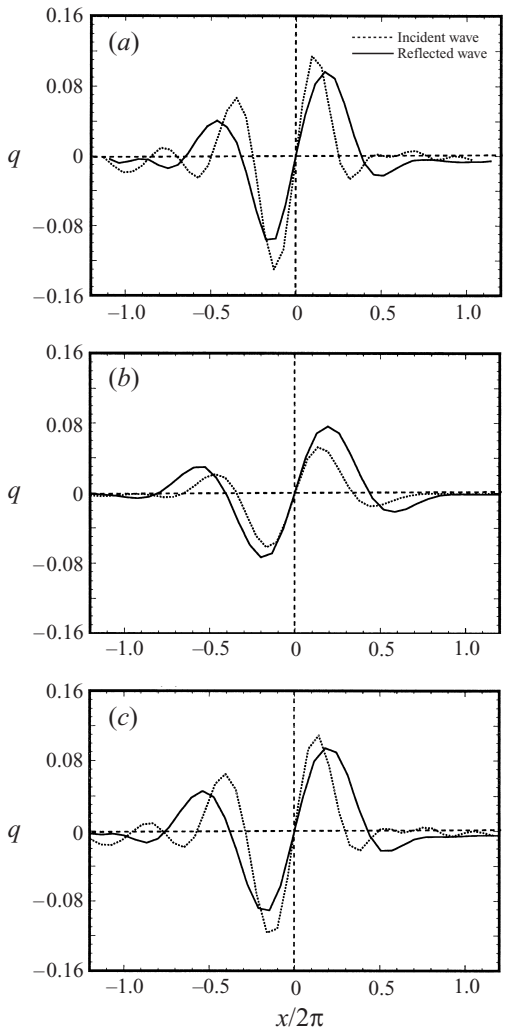

FIGURE 3. The waveforms of the internal wave before and after the reflection; $\alpha = 45$, $\beta = 10$, $Ri = 2$, $Pr = 7$, $T = 17$. No phase shift occurs when internal waves reflect. (*a*) $Ke = 10^{-4}$, $Re = 10^6$; (*b*) $Ke = 10^{-4}$, $Re = 5000$; (*c*) $Ke = 0.3$, $Re = 10^6$.

Re	Ke	C_r
5000	0.0001	0.34
100 00	0.0001	0.51
200 00	0.0001	0.67
500 00	0.0001	0.83
100 000	0.0001	0.92
100 000	0.0015	0.91
100 000	0.02	0.90
100 000	0.3	0.82

TABLE 2. Reflection coefficients for the different Keulegan and Reynolds numbers.

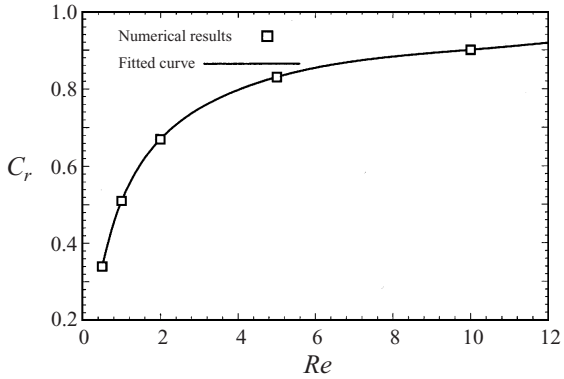

FIGURE 4. The reflection coefficient approaches unity with an increasing Reynolds number; $\alpha = 45$, $\beta = 10$, $Ri = 2$, $Ke = 0.0001$, $Pr = 7$.

α	β	Ri	ω/ω_c	C_r
40	10	2.4	3.70	0.90
40	15	2.4	2.48	0.69
40	20	2.4	1.88	0.58
40	25	2.4	1.52	0.35
45	10	2.0	4.07	0.85
45	15	2.0	2.73	0.78
45	20	2.0	2.07	0.64
45	25	2.0	1.67	0.57
45	30	2.0	1.41	0.40
50	10	1.7	4.41	0.78
50	15	1.7	2.96	0.82
50	20	1.7	2.24	0.74
50	25	1.7	1.81	0.57
50	30	1.7	1.53	0.40
50	35	1.7	1.34	0.22

TABLE 3. Reflection coefficients for the different frequencies; $Ke = 1.0 \times 10^{-4}$, $Re = 2.5 \times 10^4$.

is the ratio between the energy flux density of the reflected waves and the incident waves. Here p_i and q_i are the pressure and normal velocity along the incident ray and p_r and q_r are the pressure and normal velocity along the reflected ray. The present results show that the reflection coefficient increases with decreasing Keulegan number and increasing Reynolds number (table 2), and approaches unity (figure 4) as linear and inviscid conditions are approached.

3.1.3. *Bottom slope effect on the reflection coefficient*

To illustrate the effect of the bottom slope on the reflection coefficient we performed the simulations for the range of $1.34 \leqslant \omega/\omega_c \leqslant 4.4$ (table 3) with constant values of $Re = 25\,000$ and $Ke = 0.0001$. At the critical frequency ($\omega/\omega_c = 1$) the incident wave energy is trapped in the boundary region and the reflection coefficient is zero (figure 5). In this case, the reflected rays propagate along the sloping boundary. As the angle of the incident rays to the horizontal increases, the angle of the reflected rays to the sloping boundary also increases until the ray reflects back into the incident

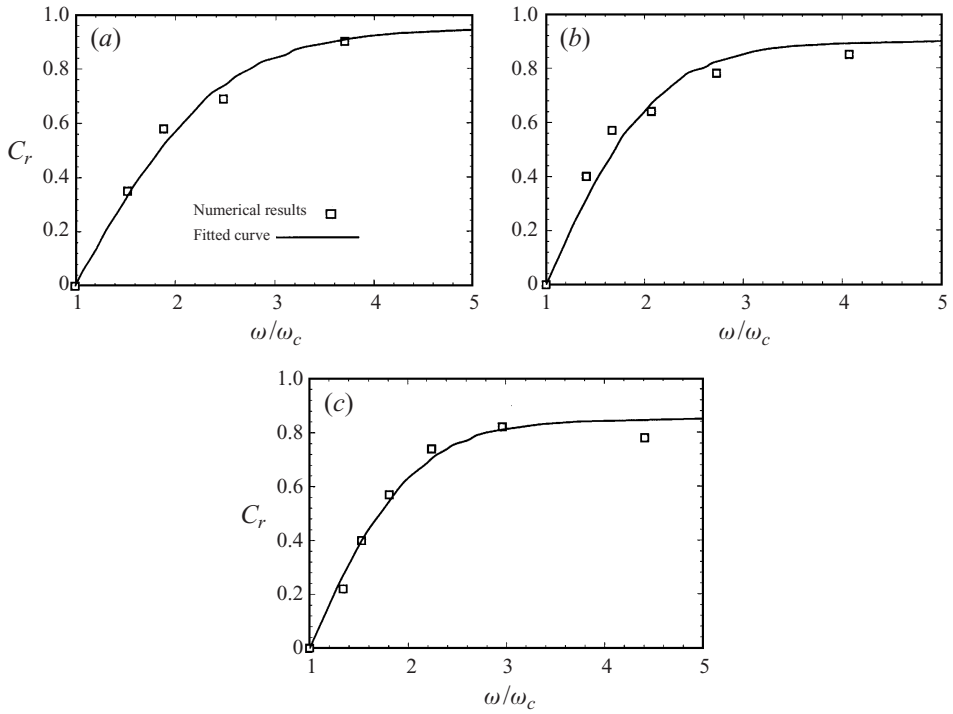

FIGURE 5. The reflection coefficient increases by departure from the critical frequency and approaches unity at $\omega/\omega_c = \infty$. (*a*) $\alpha = 40$, (*b*) $\alpha = 45$, (*c*) $\alpha = 50$.

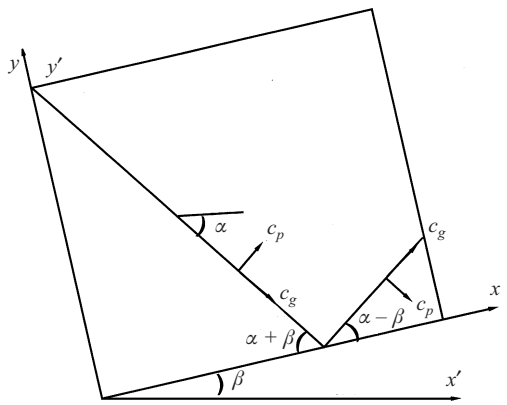

FIGURE 6. As the angle of the incident rays to the horizontal increases, the angle of the reflected rays to the sloping boundary also increases until the ray reflects back into the incident ray.

ray. It follows that (figure 6)

$$\alpha + \beta = \alpha - \beta, \quad \pi - [(\alpha + \beta) + (\alpha - \beta)] = 0, \tag{3.2}$$

so that

$$\beta = 0, \quad \alpha = \pi/2. \tag{3.3}$$

This is the reflection from a flat bottom, and is expected to be unity for the linear case. The reflection coefficient increases by departure from the critical frequency and approaches unity at $\omega/\omega_c = \sin(\alpha)/\sin(\beta) = \sin(\pi/2)/\sin(0) = \infty$ (figure 5).

α	β	Ke	Re	Dissipation equation (1.17)	Dissipation numerical results
40	10	1.0×10^{-4}	2.5×10^{4}	0.12×10^{-13}	0.14×10^{-13}
40	15	1.0×10^{-4}	2.5×10^{4}	0.44×10^{-13}	0.46×10^{-13}
40	20	1.0×10^{-4}	2.5×10^{4}	0.90×10^{-13}	0.89×10^{-13}
40	25	1.0×10^{-4}	2.5×10^{4}	1.21×10^{-13}	1.23×10^{-13}
45	10	1.0×10^{-4}	2.5×10^{4}	0.24×10^{-13}	0.25×10^{-13}
45	15	1.0×10^{-4}	2.5×10^{4}	0.52×10^{-13}	0.51×10^{-13}
45	20	1.0×10^{-4}	2.5×10^{4}	1.05×10^{-13}	1.08×10^{-13}
45	25	1.0×10^{-4}	2.5×10^{4}	1.60×10^{-13}	1.62×10^{-13}
45	30	1.0×10^{-4}	2.5×10^{4}	1.76×10^{-13}	1.78×10^{-13}
45	10	1.0×10^{-4}	1.0×10^{5}	0.22×10^{-13}	0.25×10^{-13}
45	10	1.0×10^{-4}	5.0×10^{4}	0.42×10^{-13}	0.41×10^{-13}
45	10	1.0×10^{-4}	2.0×10^{4}	0.77×10^{-13}	0.75×10^{-13}
45	10	1.0×10^{-4}	1.0×10^{4}	0.98×10^{-13}	0.95×10^{-13}
45	10	1.0×10^{-4}	5.0×10^{3}	1.02×10^{-13}	1.00×10^{-13}
45	10	1.5×10^{-3}	1.0×10^{5}	5.01×10^{-12}	5.05×10^{-12}
45	10	2.0×10^{-2}	1.0×10^{5}	9.97×10^{-10}	9.95×10^{-10}
45	10	3.0×10^{-1}	1.0×10^{5}	3.62×10^{-07}	3.45×10^{-07}
50	10	1.0×10^{-4}	2.5×10^{4}	0.55×10^{-13}	0.59×10^{-13}
50	15	1.0×10^{-4}	2.5×10^{4}	0.91×10^{-13}	0.93×10^{-13}
50	20	1.0×10^{-4}	2.5×10^{4}	1.59×10^{-13}	1.55×10^{-13}
50	25	1.0×10^{-4}	2.5×10^{4}	2.36×10^{-13}	2.33×10^{-13}
50	30	1.0×10^{-4}	2.5×10^{4}	2.59×10^{-13}	2.58×10^{-13}
50	35	1.0×10^{-4}	2.5×10^{4}	2.23×10^{-13}	2.30×10^{-13}

TABLE 4. Dissipation for the different numerical parameters.

In order to evaluate the average dissipation within the benthic region, we have calculated the average dissipation using (1.17), obtained by Ivey *et al.* (1995), and also using instantaneous velocity gradients for different numerical conditions; q, C_r and instantaneous velocity gradients were obtained from the numerical results. The numerical results confirm for the cases of incipient breaking (table 4) the relationship suggested by Ivey *et al.* (1995). It is clear that the numerical dissipation was only a small fraction ($< 16\%$) of the physical dissipation as noted by Javam *et al.* (1999*b*), the maximum being reached once small scales had fully formed and the flow became three-dimensional. Based on the highest dissipation in our simulations the Kolmogorov scale L_k is 0.017π. Cowen & Monismith (1997) showed that 99% of the dissipation takes place within the scales greater than $5.5L_k = 0.094\pi$, therefore the present model with largest grid size of 0.1π is expected to be able to resolve effectively the dominant large-scale flow features. This is of course no longer the case once full breaking takes place at higher Reynolds number.

3.2. *Wave–wave interaction*

3.2.1. *Evolution of the density field*

Figure 7 contains a sequence of plots taken at an intermediate time depicting the evolution of the density field with time T, where the time is in wave periods ($T = t/2\pi$). The density field is indicated by contour lines, and regions of density overturning (i.e. where $\mathrm{d}(\rho + \hat{\rho})/\mathrm{d}y \geqslant 0$) are shown as enclosed areas. As seen from the figure the amplitude of the resultant wave, within the interaction region, increases

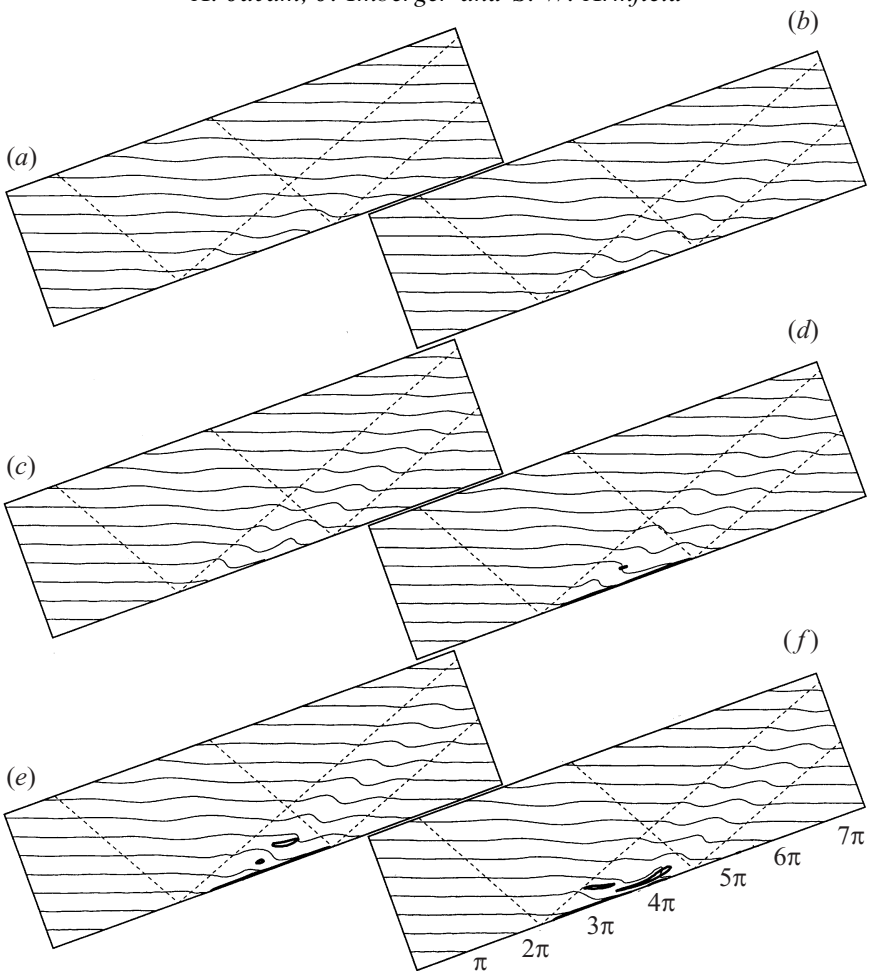

FIGURE 7. Density contours; $\alpha = 40$, $\beta = 20$, $Ri = 2$, $Ke = 0.5$, $Pr = 7$, $Re = 25\,000$. Density overturning occurs when the wave amplitude becomes large. Enclosed areas indicate regions of density overturning. (*a*) $t = 7.0$, (*b*) $t = 9.0$, (*c*) $t = 11.0$, (*d*) $t = 12.35$, (*e*) $t = 13.5$, (*f*) $t = 15.0$.

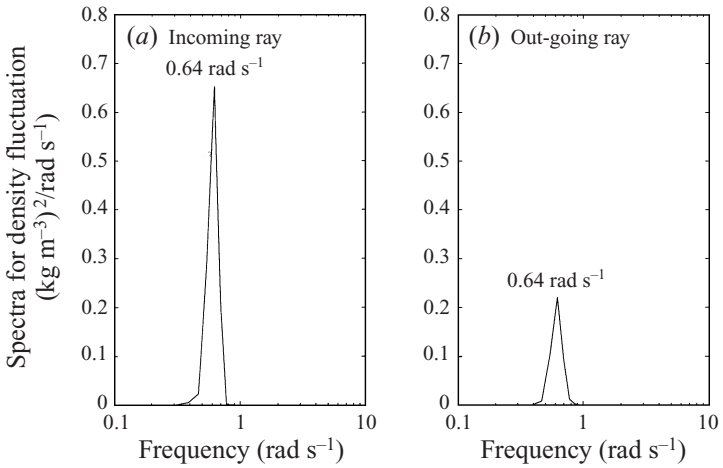

FIGURE 8. Spectra for density fluctuations; $\alpha = 40$, $\beta = 30$, $Ri = 2$, $Ke = 0.7$, $Pr = 7$, $Re = 20\,000$.

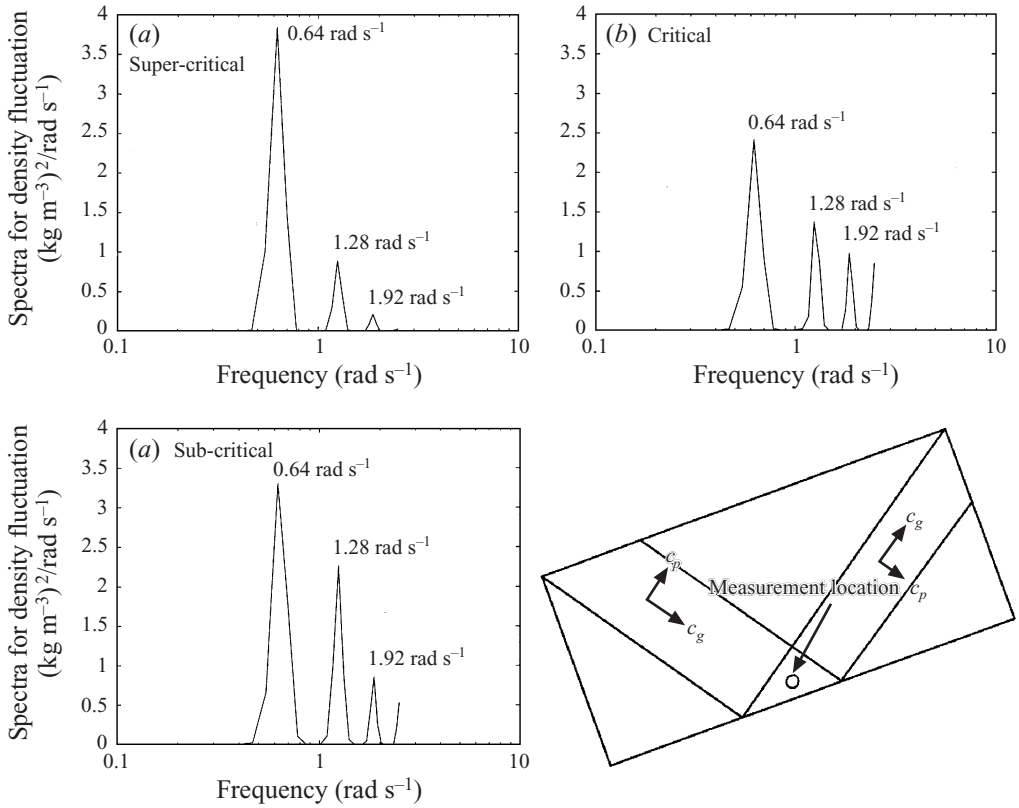

FIGURE 9. Spectra for density fluctuations; $\alpha = 40$, $Ri = 2$, $Ke = 0.7$, $Pr = 7$, $Re = 20\,000$. Higher modes are excited, the same as wave–wave interaction.

with time until a density overturn occurs. The amplitude increase associated with this effect is similar to symmetric wave–wave interaction (Teoh, Ivey & Imberger 1997; Javam *et al.* 1999*b*). The first overturned region is apparent near the centre of the interaction region (figure 7*d*) and propagates upslope at the x-component of the incident phase speed. With increased time (figure 7*f*) the motion within the overturned regions breaks down into small-scale motions and the overall region with overturns becomes larger.

3.2.2. *Production of new modes and superharmonic instability*

Density fluctuation spectra for locations inside the incoming ray, inside the outgoing ray, and inside the interaction region were used to investigate the production of new modes by nonlinear interactions of these rays. Density fluctuation spectra for the locations inside the incident and the reflected rays confirm the fundamental results of the linear theory; frequency is preserved upon reflection (figure 8).

Figure 9 shows results from the interaction region and it is clear that there was substantial wave energy at the frequencies $n\omega$, where $n = 2, 3, \ldots$. The $n > 2$ modes must be produced locally as the wave energy inside the incident ray is only at the frequency of ω. The new modes do not satisfy the dispersion relation and are therefore forced oscillations sustained locally by the nonlinear terms in the equation of motion. Thus, the nonlinear non-resonant interactions between the

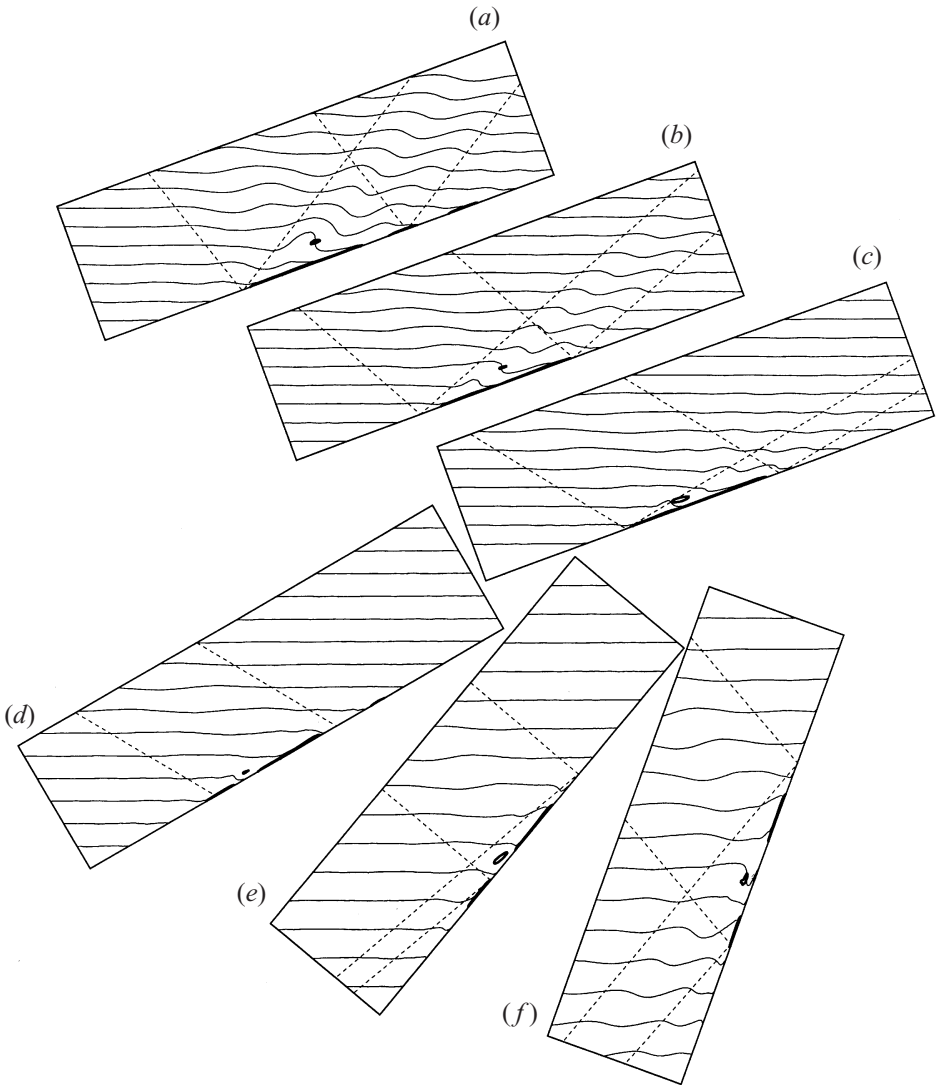

FIGURE 10. Density contours. Close to the critical frequency the wave overturning occurs at the wall. As α increases or decreases from the critical angle the wave overturning begins to depart from the wall. (*a*) $\alpha = 50$, $\beta = 20$, $Ke = 0.5$, $t = 11.5$; (*b*) $\alpha = 40$, $\beta = 20$, $Ke = 0.5$, $t = 12.25$; (*c*) $\alpha = 30$, $\beta = 20$, $Ke = 0.8$, $t = 9.25$; (*d*) $\alpha = 30$, $\beta = 30$, $Ke = 0.8$, $t = 5.75$; (*e*) $\alpha = 40$, $\beta = 50$, $Ke = 0.5$, $t = 6.75$; (*f*) $\alpha = 50$, $\beta = 70$, $Ke = 0.5$, $t = 12.0$.

incident and reflected wave rays are responsible for transferring energy from the forcing frequency to the higher harmonics. As the frequencies of the excited harmonics are greater than the local buoyancy frequency N, these modes cannot propagate out of the interaction region. The trapped energy increased with time and subsequently lead to superharmonic instabilities identical to what was observed in symmetric wave–wave interaction (Javam *et al.* 1999*b*; Teoh *et al.* 1997) and at a turning point in a shear (Javam *et al.* 1999*a*), but quite different to what was observed at a caustic reflection where the modes produced are subharmonics (Javam *et al.* 1999*a*).

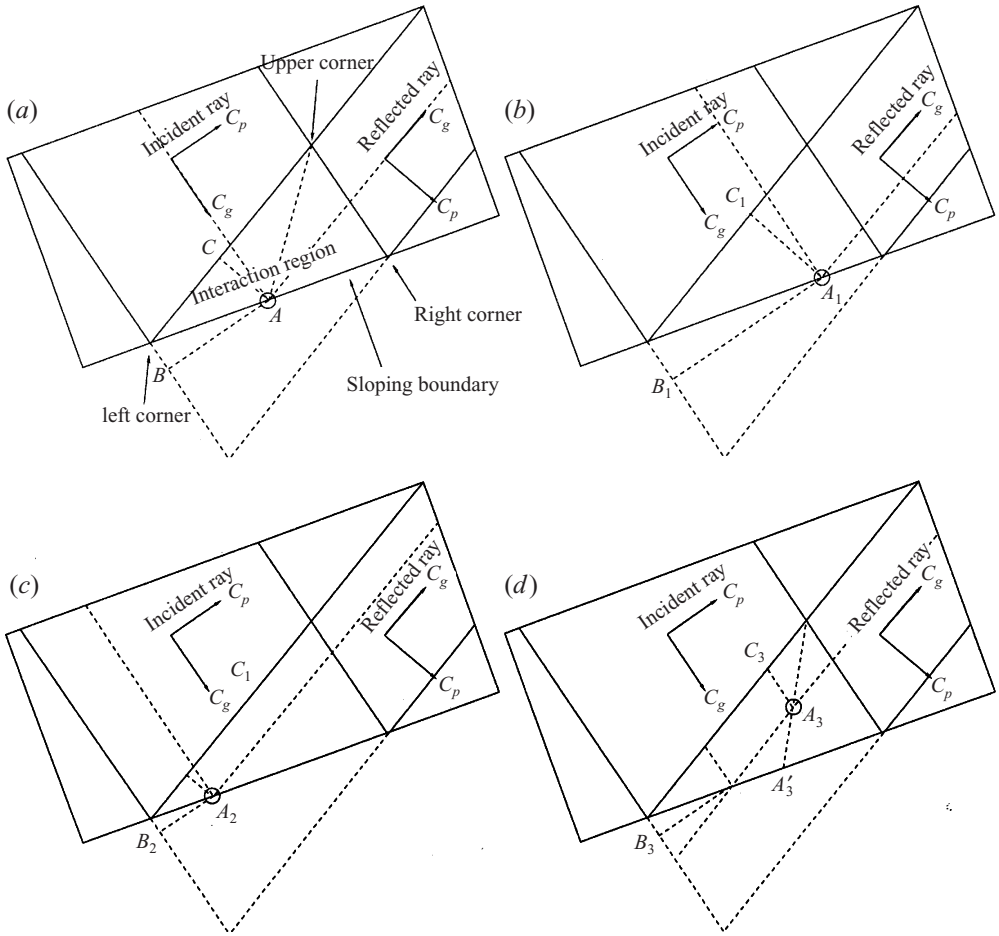

FIGURE 11. The location and size of the unstable region is determined by the amount of the energy contributed from the incident and reflected waves. As A moves up the wall the contribution (BA) from the incident ray and (CA) from the reflected ray both increase.

3.2.3. *Location of the unstable region*

The results showed that the location of the unstable region depended on the wave frequency and slope angle. To examine this effect, simulations were performed using different slopes and frequencies. The results are displayed in figure 10. The height of the interaction region increased with increasing forcing frequency. Close to the critical frequency (with zero interaction height) the wave overturning occurred near the wall. As α was increased or decreased from the critical value, the wave overturning began to lift off from the wall. However, as time continued the unstable region extended down to the boundary (figure 7*f*). This sequence of events was also observed by De Silva *et al.* (1997) in laboratory experiments.

The overturning occurred on the reflection side and propagated along the reflection side of the interaction region. To explore the underlying reason, consider point A in figure 11(*a*). Energy is contributed by both the incident and reflected rays. As the incident wave travels the distance from B to A while the reflected wave travels from

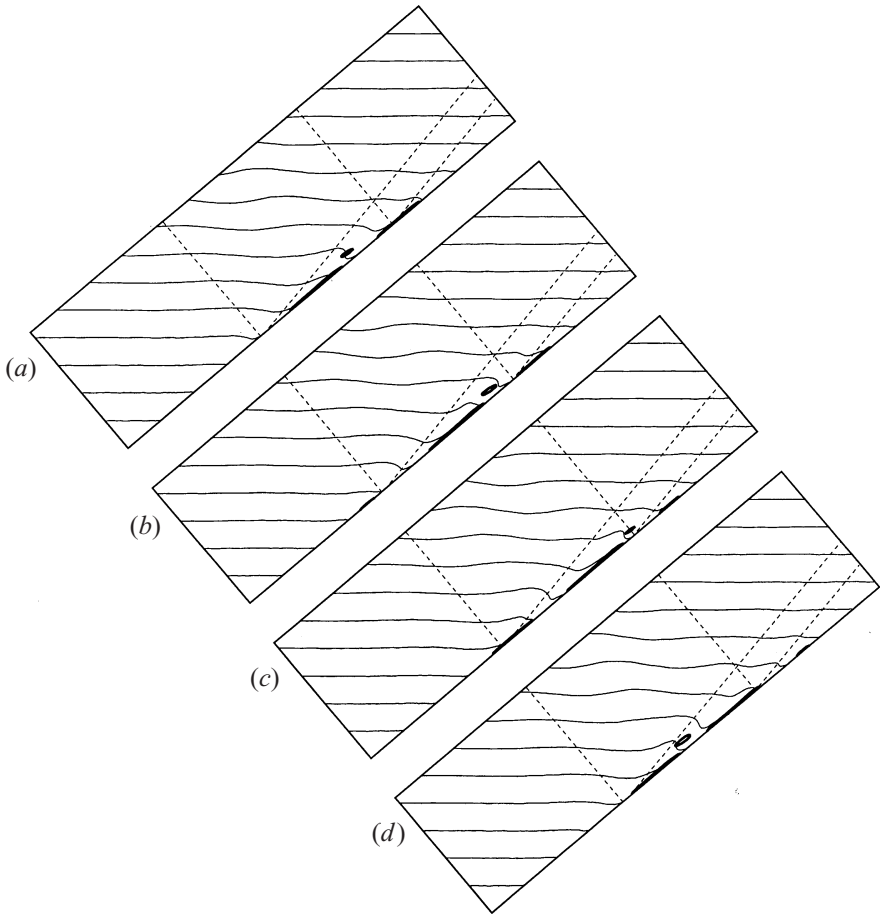

FIGURE 12. Density contours; $\alpha = 50$, $\beta = 40$, $Ri = 1.7$, $Ke = 0.35$, $Pr = 7$, $Re = 25\,000$. Density overturning occurs in the upper half of the interaction region for the supercritical case. (*a*) $t = 6.75$, (*b*) $t = 7.0$, (*c*) $t = 7.25$, (*d*) $t = 7.5$.

C to A, it follows that the total energy contributed to an unstable region at this point is proportional to

$$\frac{BA}{\text{incident raywidth}} \times E_i + \frac{CA}{\text{reflected raywidth}} \times E_r. \tag{3.4}$$

In the supercritical case (figure 11), both BA and CA increased as point A moved upslope (figure 11*b*; $BA < B_1A_1$ and $CA < C_1A_1$), and decreased as A moved downslope (figure 11*c*; $BA > B_2A_2$ and $CA > C_2A_2$) or by lifting off from the boundary (figure 11*d*; $BA > B_3A_3'$ and $CA > C_3A_3$). It follows that, if there is to be sufficient energy, the overturning must occur towards the right-hand side of the interaction region (figure 12), where the total energy contributed increases until it becomes sufficient. The same argument can be applied to the critical case where the overturning occurs in the middle (figure 13), and to subcritical reflection where the overturning is towards the left-hand side of the region (figure 14).

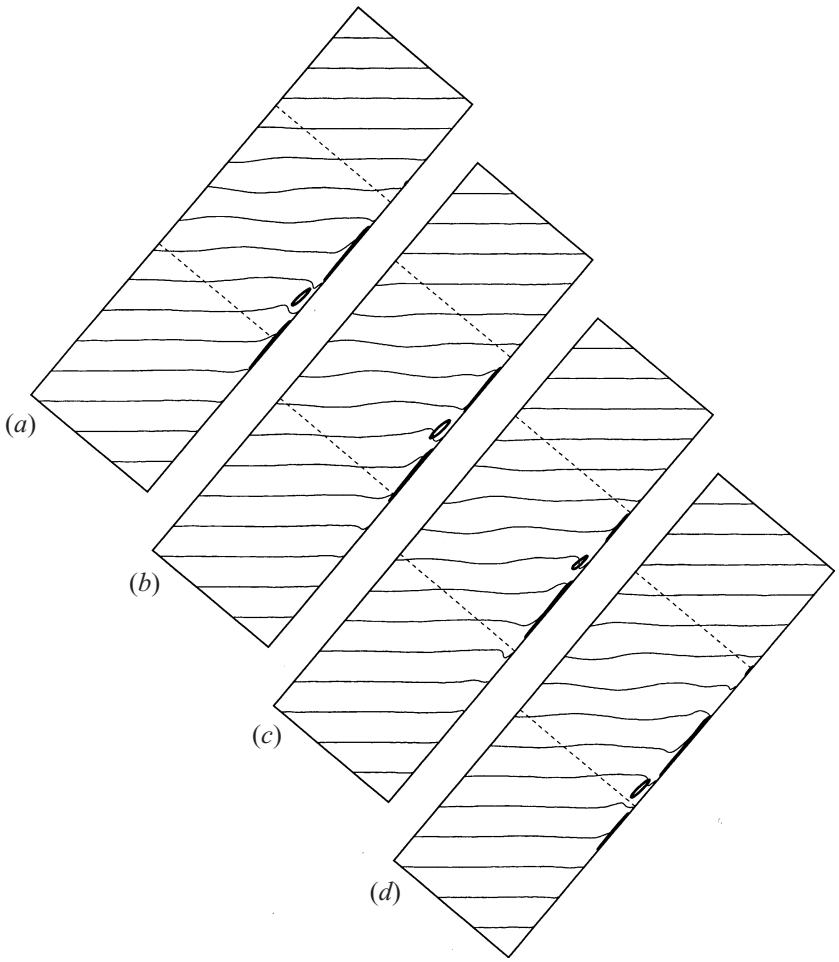

FIGURE 13. Density contours; $\alpha = 50$, $\beta = 50$, $Ri = 1.7$, $Ke = 0.35$, $Pr = 7$, $Re = 25\,000$. Density overturning occurs in the mid half of the interaction region for the critical case. (*a*) $t = 7.25$, (*b*) $t = 7.5$, (*c*) $t = 7.75$, (*d*) $t = 8.0$.

4. Conclusion

In this paper the nature of the nonlinear processes induced by internal wave breaking on a sloping boundary was explored, the reflection coefficient was determined, the distribution of the wave energy near the reflection region was examined and finally typical dissipation values within the reflection region were estimated.

It has been shown that no phase shift occurred upon reflection from the slope and the reflection coefficient approached unity as nonlinearity and viscosity decreased and as the forcing frequency departed from the critical value. The nonlinear interactions transferred energy to higher modes, with associated overturning of the density field along the reflected wave. This mechanism of instability was similar to symmetric wave–wave interaction (Teoh *et al.* 1997; Javam *et al.* 1999*b*) and instability at a turning point (Javam *et al.* 1999*a*) but followed a totally different mechanism than that of wave overturning induced by caustic reflections (Javam *et al.* 1999*a*) where lower modes were produced. Close to the critical frequency, the wave overturning took place near the wall. As α increased or decreased from the critical angle, the

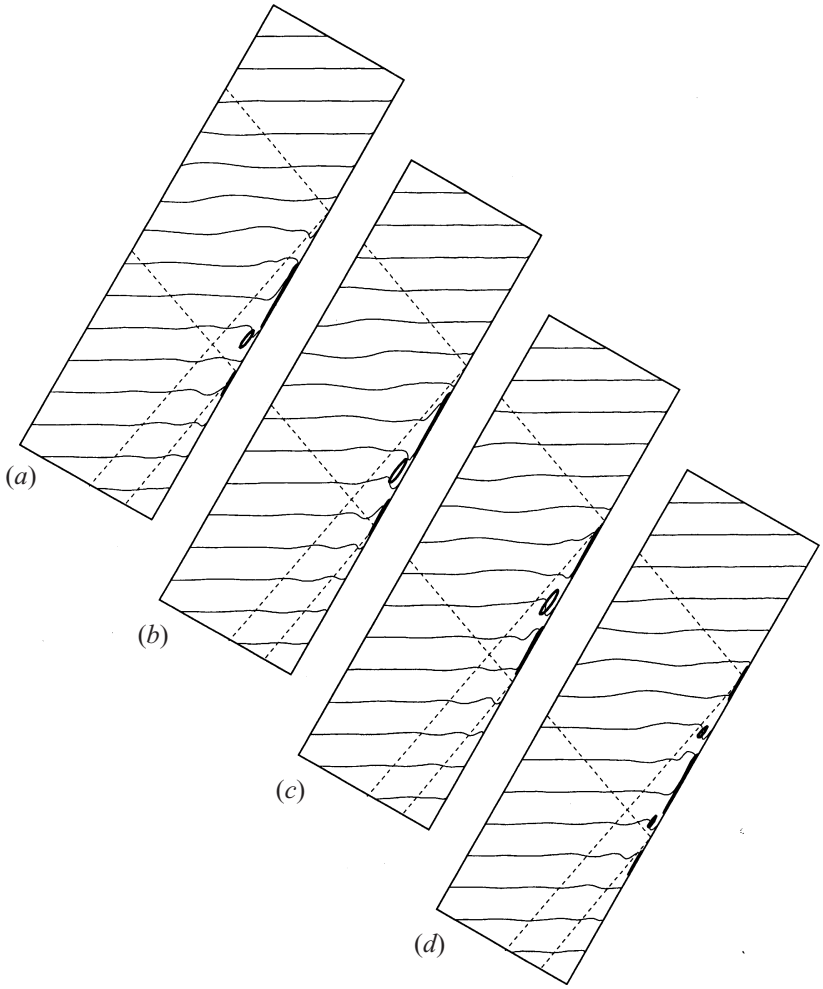

FIGURE 14. Density contours; $\alpha = 50$, $\beta = 60$, $Ri = 1.7$, $Ke = 0.35$, $Pr = 7$, $Re = 25\,000$. Density overturning occurs in the lower half of the interaction region for the subcritical case. (*a*) $t = 10.75$, (*b*) $t = 11.0$, (*c*) $t = 11.25$, (*d*) $t = 11.5$.

overturning departed from the wall and was located on the reflection side of the interaction region.

We wish to thank the Centre for Environmental Fluid Dynamics (CEFD) for providing extensive computer resources and financial support. This is Environmental Dynamics contribution ED-875-AJ.

REFERENCES

ARMFIELD, S. W. 1991 Finite difference solutions of the Navier–Stokes equations on staggered and non-staggered grids. *Computers Fluids* **20**, 1–17.

ARMFIELD, S. W. 1994 Ellipticity, accuracy and convergence of the discrete Navier–Stokes equations. *J. Comput. Phys.* **114**, 176–184.

ARMI, L. 1978 Some evidence of boundary mixing in the deep ocean. *J. Geophys. Res.* **83**, 1971–1979.

COWEN, E. A. & MONISMITH, S. G. 1997 A hybrid digital particle tracking velocimetry technique. *Exps. Fluids* **22**, 199–211.

De Silva, I. P. D., Imberger, J. & Ivey, G. N. 1997 Localised mixing due to a breaking internal wave ray at a sloping bed. *J. Fluid Mech.* **350**, 1–27.

Eriksen, C. C. 1982 Observations internal wave reflection off sloping bottoms. *J. Geophys. Res.* **87**, 525–538.

Eriksen, C. C. 1985 Implications of ocean bottom reflection for internal wave spectra and mixing. *J. Phys. Oceanogr.* **15**, 1145–1156.

Eriksen, C. C. 1997 Internal wave reflection and mixing at Fieberling Guyot. *J. Geophys. Res.* Submitted.

Garrett, C. 1990 The role of secondary circulation in boundary mixing. *J. Geophys. Res.* **95**, 3181–3188.

Gregg, M. C. & Sanford, T. B. 1980 Signature of Mixing from the Bernoda slope, the Sargasso sea and the Gulf Stream. *J. Phys. Oceanogr.* **10**, 105–127.

Imberger, J. 1989 Vertical heat flux in the hypolimnion of a lake. In *Proc. 10th AFMC, Melbourne*, vol. I, pp. 2.13–2.16.

Imberger, J. 1994 Transport processes in lakes: a review. In *Limnology Now: a Paradigm of Planetary Problems* (ed. R. Margalef), pp. 99–123. Elsevier.

Ivey, G. N. 1987 Boundary mixing in a rotating stratified fluid. *J. Fluid Mech.* **183**, 25–44.

Ivey, G. N., De Silva, I. D. P & Imberger, J. 1995 Internal waves, bottom slopes and boundary mixing. In *Proc. 'Aha Huliko' A Hawaiian Winter workshop. University of Hawaii*, pp. 199–206.

Ivey, G. N. & Nokes, R. I. 1989 Vertical mixing due to the breaking of critical internal waves on sloping boundaries. *J. Fluid Mech.* **204**, 479–500.

Javam, A., Imberger, J. & Armfield, S. W. 1999*a* Numerical study of internal wave–wave interaction in a stratified fluid. *J. Fluid Mech.* submitted.

Javam, A., Imberger, J & Armfield, S. W. 1999*b* Numerical study of internal wave-caustic and internal wave-shear interactions in a stratified fluid. *J. Fluid Mech.* submitted.

Ledwell, J. R. & Watson, A. J. 1991 The Santa Monica Basin tracer experiment: A study of diapycnal and isopycnal mixing. *J. Geophys. Res.* **96**, 8695–8718.

Patankar, S. 1980 *Numerical Heat Transfer and Fluid Flow*. Hemisphere.

Phillips, O. M. 1977 *The Dynamics of the Upper Ocean*. Cambridge University Press.

Phillips, O. M., Shyu, J. H. & Salmun, H. 1986 An experiment on boundary mixing: mean circulation and transport rate. *J. Fluid Mech.* **173**, 473–499.

Salmun, H., Killworth, P. D. & Blundell, J. R. 1991 A two-dimensional model of boundary mixing. *J. Geophys. Res.* **96**, 18447–18474.

Slinn, D. N. & Riley, J. J. 1996 Turbulent mixing in the oceanic boundary layer due to internal wave reflection from sloping terrain. *Dyn. Atmos. Oceans* **23**, 51–62.

Taylor, J. 1993 Turbulence and mixing in the boundary layer generated by shoaling internal waves. *Dyn. Atmos. Oceans* **19**, 233–258.

Teoh, S. G., Ivey, G. N. & Imberger, J. 1997 Experimental study of two intersecting internal waves. *J. Fluid Mech.* **336**, 91–122.

Thorpe, S. A. 1987 On the reflection of a train of finite-amplitude internal waves from uniform slope. *J. Fluid Mech.* **178**, 279–302.